Stability of the resistive wall mode in HBT-EP plasmas

Richard Fitzpatrick and James Bialek

Citation: Physics of Plasmas (1994-present) **13**, 072512 (2006); doi: 10.1063/1.2245542
View online: http://dx.doi.org/10.1063/1.2245542
View Table of Contents: http://scitation.aip.org/content/aip/journal/pop/13/7?ver=pdfcov
Published by the AIP Publishing

Stability of the resistive wall mode in HBT-EP plasmas

Richard Fitzpatrick
Institute for Fusion Studies, Department of Physics, University of Texas at Austin, Austin, Texas 78712

James Bialek
Department of Applied Physics and Applied Mathematics, Columbia University, New York, New York 10027

(Received 25 April 2006; accepted 10 July 2006; published online 31 July 2006)

A relatively simple model of the resistive wall mode (RWM) is derived for a large aspect ratio, low β, circular cross section, tokamak plasma, surrounded by a concentric, thin, uniform resistive wall. The model employs uniform toroidal plasma rotation, and includes the following realistic edge dissipation mechanisms: dissipation due to charge-exchange with cold neutrals, and dissipation due to neoclassical flow damping. The model is applied to the HBT-EP tokamak [T. Ivers, E. Eisner, A. Garofalo *et al.*, Phys. Plasmas **3**, 1926 (1996)], with the wall parameters determined by fitting to output from the VALEN code [J. Bialek, A. H. Boozer, M. E. Mauel, and G. A. Navratil, Phys. Plasmas **8**, 2170 (2001)]. Dissipation due to charge-exchange with cold neutrals is found to be not quite large enough to account for the observed rotational stabilization of the RWM in HBT-EP plasmas. On the other hand, dissipation due to neoclassical flow damping is sufficiently large to explain the observations. © *2006 American Institute of Physics*. [DOI: 10.1063/1.2245542]

I. INTRODUCTION

The promising "advanced tokamak" (AT) concept is only economically attractive provided that the ideal external kink β limit[1] is raised substantially due to the presence of a close-fitting electrically conducting wall, surrounding the plasma.[2,3] This, in turn, is only possible provided that the so-called *resistive wall mode*[4] (RWM) is somehow stabilized. Various tokamak experiments have established that the RWM can be stabilized via rapid plasma rotation.[5–8] According to conventional theory,[9,10] this stabilization is a combined effect of plasma *rotational inertia* and plasma *dissipation*.

Previously, a simple cylindrical model of the RWM was introduced in which the requisite plasma dissipation was provided by edge perpendicular viscosity.[11] In this paper, we outline an improved version of this model which assesses two additional, and much more realistic, edge dissipation mechanisms, namely, flow damping due to charge-exchange with cold neutrals,[12,13] and neoclassical flow damping.[14,15]

The RWM arises in a tokamak plasma when an ideal external-kink mode,[16] is stable in the presence of a close-fitting *perfectly conducting* wall, but unstable in the absence of such a wall. In the presence of a realistic wall possessing a *finite* electrical resistivity, the stabilized external-kink mode is converted into the possibly unstable, but relatively slowly growing, RWM.[4] As has already been mentioned, a combination of plasma rotation and plasma dissipation can stabilize the RWM. In the absence of RWM stabilization, the effective stability boundary for the plasma is the so-called *no-wall stability boundary*, which is the ideal external-kink stability boundary calculated in the absence of a wall. On the other hand, if the RWM is completely stabilized then the effective stability boundary for the plasma becomes the so-called *perfect-wall stability boundary*, which is the ideal external-kink stability boundary calculated under the assumption that the wall is perfectly conducting.

In practice, ideal external-kink modes in tokamaks are driven by plasma *pressure gradients*.[1] Hence, the two above-mentioned stability limits translate into two limiting values of β (i.e., the ratio of the plasma energy density to the magnetic energy density), namely, the *no-wall* β *limit*, $\beta_{\rm nw}$, and the *perfect-wall* β *limit*, $\beta_{\rm pw}$. In general, $\beta_{\rm pw}$ is significantly larger than $\beta_{\rm nw}$ in advanced tokamak scenarios. If β_c is the actual β limit in the presence of a resistive wall, then we can define a convenient figure of merit,

$$\bar{s} = \frac{\beta_c - \beta_{\rm nw}}{\beta_{\rm pw} - \beta_{\rm nw}}. \tag{1}$$

Thus, if $\bar{s}=0$ then there is no stabilization of the RWM, and if $\bar{s}=1$ then the RWM is completely stabilized. The advance tokamak scenario is premised on the assumption that $\bar{s}$ can be made fairly close to unity.

Note that the ideal external-kink mode is driven by *current gradients*, rather than pressure gradients, in the cylindrical model of the RWM presented in this paper. Nevertheless, we can define an analogous figure of merit to that specified in Eq. (1) (see Sec. III D).

This paper is organized as follows: In Sec. II, we derive the ideal eigenmode equation which governs the perturbed plasma displacement associated with a RWM in a large aspect ratio, low β, circular cross section, tokamak plasma. In Sec. III, we obtain the RWM dispersion relation when such a plasma is surrounded by a concentric, thin, uniform resistive wall. The HBT-EP tokamak[17] is described in Sec. IV. In Sec. V, we assess whether edge dissipation due to charge-exchange with cold neutrals is a sufficiently large effect to account for the observed stabilization of the RWM in HBT-EP plasmas. A similar assessment is performed for edge dissipation due to neoclassical flow damping in Sec. VI. In Sec. VII, we examine the dependence of the RWM stability boundary on the details of the plasma equilibrium and the wall configuration. Finally, the paper is summarized, and conclusions are drawn, in Sec. VIII.

II. DERIVATION OF IDEAL EIGENMODE EQUATION

A. Coordinates

We adopt the standard cylindrical polar coordinates (r,θ,z). Let $\theta=0$ correspond to the outboard midplane. The system is assumed to be periodic in the z direction, with periodicity length $2\pi R_0$, where R_0 is the simulated plasma major radius. It is convenient to define a simulated toroidal angle $\varphi=z/R_0$.

B. Normalization

Unless otherwise indicated, all lengths in this paper are normalized to the plasma minor radius a, all magnetic field strengths to the toroidal field strength on the magnetic axis B_z, all masses to $\rho_0 a^3$, where ρ_0 is the plasma mass density on the magnetic axis, and all times to the Alfvén time $\tau_A=a\sqrt{\mu_0\rho_0}/B_z$.

C. Equilibrium

Consider a standard, large aspect ratio, low β, circular cross section tokamak plasma.[18] The magnetic field is written $\mathbf{B}=[0,\epsilon/q,(1+\epsilon\cos\theta)^{-1}]+O(\epsilon_0^2)$, where $q(r)$ is the safety factor, $\epsilon_0\equiv a/R_0\ll 1$ is the inverse aspect ratio, and $\epsilon=r\epsilon_0$. Let us assume, for the sake of convenience, that the plasma equilibrium is *force-free*, with current density $\mathbf{J}=\epsilon_0(\sigma/B)\mathbf{B}$, where

$$\sigma(r)=\frac{1}{r}\frac{d}{dr}\left(\frac{r^2}{q}\right)+O(\epsilon_0). \tag{2}$$

Note that, since the equilibrium is force-free, there is zero equilibrium pressure gradient, and, hence, zero diamagnetic current.

D. Perturbed equations

Consider a plasma instability governed by the following set of linearized ideal magnetohydrodynamical equations

$$\gamma'\tilde{\mathbf{b}}=\nabla\times(\tilde{\mathbf{v}}\times\mathbf{B}), \tag{3}$$

$$(\gamma'+\nu)\rho\tilde{\mathbf{v}}=-\nabla\tilde{p}-\nabla\cdot\tilde{\mathbf{\Pi}}_{\parallel}+\tilde{\mathbf{j}}\times\mathbf{B}+\mathbf{J}\times\tilde{\mathbf{b}}, \tag{4}$$

$$\gamma'\tilde{p}=-\rho c_s^2\nabla\cdot\tilde{\mathbf{v}}. \tag{5}$$

Here, $\tilde{}$ denotes a perturbed quantity, $\tilde{\mathbf{b}}$ is the perturbed magnetic field, $\tilde{\mathbf{j}}$ is the perturbed current density, $\tilde{\mathbf{v}}$ is the perturbed plasma velocity, $\tilde{p}$ is the perturbed plasma pressure, $\tilde{\mathbf{\Pi}}_{\parallel}$ is the perturbed plasma parallel stress tensor, γ' is the mode growth rate in the plasma frame, $\rho(r)$ is the equilibrium plasma mass density, $c_s(r)$ is the plasma sound speed, and $\nu(r)$ is a phenomenological plasma flow-damping rate (which will be used to represent flow damping due to charge-exchange with neutrals). Note that we have neglected plasma resistivity [since there is no rational surface inside the plasma for a cylindrical RWM (Ref. 16)], the plasma gyroviscous and perpendicular stress tensors (since these are both much smaller than the parallel stress tensor[19]), and equilibrium flow shear (for the sake of convenience). Furthermore, $\nabla\cdot\tilde{\mathbf{b}}=0$, $\tilde{\mathbf{j}}=\nabla\times\tilde{\mathbf{b}}$, and $\nabla\cdot\tilde{\mathbf{j}}=0$, according to Maxwell's equations.

The perpendicular component of the plasma equation of motion, Eq. (4), yields

$$\tilde{\mathbf{j}}_{\perp}=\epsilon_0\frac{\sigma}{B}\tilde{\mathbf{b}}_{\perp}+\tilde{\mathbf{j}}_{\perp p}+\tilde{\mathbf{j}}_{\perp nc}, \tag{6}$$

where

$$\tilde{\mathbf{j}}_{\perp p}=(\gamma'+\nu)\rho\frac{\mathbf{n}\times\tilde{\mathbf{v}}}{B} \tag{7}$$

is the perturbed polarization current, and

$$\tilde{\mathbf{j}}_{\perp nc}=\frac{\mathbf{n}\times(\nabla\tilde{p}+\nabla\cdot\tilde{\mathbf{\Pi}}_{\parallel})}{B} \tag{8}$$

is the perturbed neoclassical current. Here, $\mathbf{n}=\mathbf{B}/B$.

The parallel component of Eq. (4) gives

$$(\gamma'+\nu)\rho\tilde{v}_{\parallel}=-\mathbf{n}\cdot\nabla\tilde{p}-\mathbf{n}\cdot\nabla\cdot\tilde{\mathbf{\Pi}}_{\parallel}. \tag{9}$$

E. Perturbed velocity

The perturbed velocity is written as a combination of $\mathbf{E}\times\mathbf{B}$ and parallel flow[20]

$$\tilde{\mathbf{v}}=\frac{\gamma'\nabla\tilde{\phi}\times\mathbf{n}}{B}+\tilde{v}_{\parallel}\mathbf{n}, \tag{10}$$

where $-\gamma'\tilde{\phi}$ is the perturbed scalar electric potential. It follows that

$$\nabla\cdot\tilde{\mathbf{v}}=\mathbf{n}\cdot\nabla\tilde{v}_{\parallel}-\tilde{v}_{\parallel}\mathbf{n}\cdot\nabla\ln B-2\tilde{\mathbf{v}}_{\perp}\cdot\nabla\ln B+O(\epsilon_0^2\tilde{v}_{\perp}), \tag{11}$$

and

$$(\mathbf{nn}-\overleftrightarrow{\mathbf{I}}/3):\nabla\tilde{\mathbf{v}}=\tfrac{2}{3}\mathbf{n}\cdot\nabla\tilde{v}_{\parallel}+\tfrac{1}{3}\tilde{v}_{\parallel}\mathbf{n}\cdot\nabla\ln B-\tfrac{1}{3}\tilde{\mathbf{v}}_{\perp}\cdot\nabla\ln B+O(\epsilon_0^2\tilde{v}_{\perp}). \tag{12}$$

Here, $\overleftrightarrow{\mathbf{I}}$ is the identity tensor. Incidentally, it is easily demonstrated that $\nabla\cdot\mathbf{n}=-\mathbf{n}\cdot\nabla\ln B$, $\nabla\times\mathbf{n}=\mathbf{n}\times\nabla\ln B+\epsilon_0(\sigma/B)\mathbf{n}$, and $(\mathbf{n}\cdot\nabla)\mathbf{n}=\nabla_{\perp}\ln B$.

F. Perturbed parallel stress tensor

We adopt the standard collisional form of perturbed parallel stress tensor[19,21]

$$\tilde{\mathbf{\Pi}}_{\parallel}=\tfrac{3}{2}\tilde{\pi}_{\parallel}(\mathbf{nn}-\overleftrightarrow{\mathbf{I}}/3), \tag{13}$$

where

$$\tilde{\pi}_{\parallel}=-2\eta_0(\mathbf{nn}-\overleftrightarrow{\mathbf{I}}/3):\nabla\tilde{\mathbf{v}}. \tag{14}$$

Here, η_0 is the parallel ion viscosity. It follows that

$$\nabla\cdot\tilde{\mathbf{\Pi}}_{\parallel}=\tfrac{3}{2}\tilde{\pi}_{\parallel}\big[(\nabla\cdot\mathbf{n})\mathbf{n}+(\mathbf{n}\cdot\nabla)\mathbf{n}\big]+\tfrac{3}{2}(\mathbf{n}\cdot\nabla\tilde{\pi}_{\parallel})\mathbf{n}-\tfrac{1}{2}\nabla\tilde{\pi}_{\parallel}, \tag{15}$$

$$\mathbf{n}\cdot\nabla\cdot\tilde{\mathbf{\Pi}}_{\parallel}=-\tfrac{3}{2}\tilde{\pi}_{\parallel}\mathbf{n}\cdot\nabla\ln B+\mathbf{n}\cdot\nabla\tilde{\pi}_{\parallel}, \tag{16}$$

$$\mathbf{n}\times\nabla\cdot\tilde{\mathbf{\Pi}}_{\parallel}=\tfrac{3}{2}\tilde{\pi}_{\parallel}\mathbf{n}\times\nabla\ln B-\tfrac{1}{2}\mathbf{n}\times\nabla\tilde{\pi}_{\parallel}, \tag{17}$$

and

$$\nabla\cdot\tilde{\mathbf{j}}_{\perp nc}=\frac{\mathbf{n}\times\nabla\ln,B\cdot\nabla(\tilde{\pi}_{\parallel}+4\tilde{p})}{2B}+O(\epsilon_0^2\tilde{\pi}_{\parallel}). \tag{18}$$

Now, $B=(1+\epsilon\cos\theta)^{-1}+O(\epsilon_0^2)$, so $\nabla\ln B=\epsilon_0(-\cos\theta,\sin\theta,0)+O(\epsilon_0^2)$. Hence, Eqs. (9), (5), and (14) yield

$$(\gamma'+\nu)\rho\tilde{v}_{\parallel}=-\mathbf{n}\cdot\nabla(\tilde{p}+\tilde{\pi}_{\parallel})+\frac{3\epsilon_0}{2}\frac{\epsilon}{q}\sin\theta\tilde{\pi}_{\parallel}, \tag{19}$$

$$\gamma'\tilde{p}=-\rho c_s^2\Big(\mathbf{n}\cdot\nabla\tilde{v}_{\parallel}-\epsilon_0\frac{\epsilon}{q}\sin\theta\tilde{v}_{\parallel}-2\epsilon_0\sin\theta\tilde{v}_{\perp\theta}+2\epsilon_0\cos\theta\tilde{v}_{\perp r}+O(\epsilon_0^2\tilde{v}_{\perp})\Big), \tag{20}$$

$$\tilde{\pi}_{\parallel}=-2\eta_0\Big(\frac{2}{3}\mathbf{n}\cdot\nabla\tilde{v}_{\parallel}+\frac{\epsilon_0}{3}\frac{\epsilon}{q}\sin\theta\tilde{v}_{\parallel}-\frac{\epsilon_0}{3}\sin\theta\tilde{v}_{\perp\theta}+\frac{\epsilon_0}{3}\cos\theta\tilde{v}_{\perp r}+O(\epsilon_0^2\tilde{v}_{\perp})\Big), \tag{21}$$

respectively, and Eq. (18) reduces to

$$\nabla\cdot\tilde{\mathbf{j}}_{\perp nc}=-\frac{\epsilon_0}{2}\left[\sin\theta\frac{\partial(\tilde{\pi}_{\parallel}+4\tilde{p})}{\partial r}+\cos\theta\frac{\partial(\tilde{\pi}_{\parallel}+4\tilde{p})}{r\,\partial\,\theta}\right]+O(\epsilon_0^2\tilde{\pi}_{\parallel}). \tag{22}$$

G. Variation of perturbed quantities

Let us assume that

$$\tilde{p}(r,\theta,\varphi)=\epsilon_0\rho\big[p_0(r)+2p_c(r)\cos\theta+2p_s(r)\sin\theta\big]e^{i\zeta}, \tag{23}$$

$$\tilde{\pi}_{\parallel}(r,\theta\varphi)=\epsilon_0\rho\big[\pi_{\parallel 0}(r)+2\pi_{\parallel c}(r)\cos\theta+2\pi_{\parallel s}(r)\sin\theta\big]e^{i\zeta}, \tag{24}$$

$$\tilde{v}_{\parallel}(r,\theta,\varphi)=\big[\epsilon_0^{-1}v_{\parallel 0}(r)+2v_{\parallel c}(r)\cos\theta+2v_{\parallel s}(r)\sin\theta\big]e^{i\zeta}, \tag{25}$$

$$\tilde{\mathbf{v}}_{\perp}(r,\theta,\varphi)=\bar{\mathbf{v}}_{\perp}(r)e^{i\zeta}, \tag{26}$$

where $\zeta=m\theta-n\varphi$. In other words, the perturbed quantities $\tilde{p}$, $\tilde{\pi}_{\parallel}$, $\tilde{v}_{\parallel}$, which are all associated with *parallel* flow, are assumed to acquire sideband harmonics due to the variation of B around flux surfaces. Conversely, the perpendicular velocity $\tilde{\mathbf{v}}_{\perp}$, which drives the parallel flow, is assumed not to acquire any sideband harmonics due to the variation of B around flux surfaces. These are fairly standard assumptions in single-mode neoclassical theory.[15,21,22] It is helpful to define the average operator

$$\langle\cdots\rangle=\oint\oint(\cdots)e^{-i\zeta}\frac{d\theta}{2\pi}\frac{d\zeta}{2\pi}. \tag{27}$$

H. Calculation of $\langle\nabla\cdot\tilde{\mathbf{j}}_{\perp nc}\rangle$

Let $Q=m/q-n$, $\hat{Q}=\epsilon_0^{-1}Q$, $\Gamma_1=\epsilon_0^{-4}(\gamma'+\nu)$, $\Gamma_2=c_s^2/\gamma'$, and $\hat{\eta}_0=\eta_0/\rho$. In the following, it is assumed that $p_{0/c/s}\sim\pi_{\parallel 0/c/s}\sim v_{\parallel 0/c/s}\sim\bar{v}_{\perp}$, and $\Gamma_1\sim\Gamma_2\sim\hat{Q}\sim\hat{\eta}_0\sim q\sim O(1)$. After averaging and integration by parts in θ, Eq. (22) yields

$$\langle\nabla\cdot\tilde{\mathbf{j}}_{\perp nc}\rangle\simeq-\frac{\epsilon_0^2}{2}\left[\frac{\partial(r\rho[\pi_{\parallel s}+4p_s])}{r\,\partial\,r}+i\frac{m}{r}\rho(\pi_{\parallel c}+4p_c)\right]. \tag{28}$$

Operating on each of Eqs. (19)–(21) with each of $\langle\cdots\rangle$, $\langle\cos\theta\cdots\rangle$, and $\langle\sin\theta\cdots\rangle$, we obtain

$$\Gamma_1 v_{\parallel 0}\simeq-i\hat{Q}(p_0+\pi_{\parallel 0})+\frac{3}{2}\frac{r}{q}\pi_{\parallel s}, \tag{29}$$

$$p_s+\pi_{\parallel s}\simeq 0, \tag{30}$$

$$p_c+\pi_{\parallel c}\simeq 0, \tag{31}$$

and

$$p_0\simeq-i\Gamma_2\hat{Q}v_{\parallel 0}, \tag{32}$$

$$p_c\simeq-\Gamma_2\Big(\frac{1}{q}v_{\parallel s}+\bar{v}_{\perp r}\Big), \tag{33}$$

$$p_s\simeq-\Gamma_2\Big(-\frac{1}{q}v_{\parallel c}-\frac{1}{2}\frac{r}{q}v_{\parallel 0}-\bar{v}_{\perp\theta}\Big), \tag{34}$$

plus

$$\pi_{\parallel 0}\simeq-i\frac{4}{3}\hat{\eta}_0\hat{Q}v_{\parallel 0}, \tag{35}$$

$$\pi_{\parallel c}\simeq-\frac{2}{3}\hat{\eta}_0\left[\frac{2}{q}v_{\parallel s}+\frac{1}{2}\bar{v}_{\perp r}\right], \tag{36}$$

$$\pi_{\parallel s}\simeq-\frac{2}{3}\hat{\eta}_0\left[-\frac{2}{q}v_{\parallel c}+\frac{1}{2}\frac{r}{q}v_{\parallel 0}-\frac{1}{2}\bar{v}_{\perp\theta}\right], \tag{37}$$

respectively, to lowest order in ϵ_0.

It follows that

$$\frac{v_{\parallel c}}{q}=-\left[\frac{\Gamma_2+(1/3)\hat{\eta}_0}{\Gamma_2+(4/3)\hat{\eta}_0}\right]\bar{v}_{\perp\theta}-\frac{1}{2}\left[\frac{\Gamma_2-(2/3)\hat{\eta}_0}{\Gamma_2+(4/3)\hat{\eta}_0}\right]\frac{r}{q}v_{\parallel 0}, \tag{38}$$

$$\frac{v_{\parallel s}}{q}=-\left[\frac{\Gamma_2+(1/3)\hat{\eta}_0}{\Gamma_2+(4/3)\hat{\eta}_0}\right]\bar{v}_{\perp r}, \tag{39}$$

and

$$\pi_{\parallel c}=\frac{\hat{\eta}_0\Gamma_2}{\Gamma_2+(4/3)\hat{\eta}_0}\bar{v}_{\perp r}, \tag{40}$$

$$\pi_{\parallel s} = -\frac{\hat{\eta}_0 \Gamma_2}{\Gamma_2 + (4/3)\,\hat{\eta}_0}\left(\bar{v}_{\perp\theta} + \frac{r}{q} v_{\parallel 0}\right), \tag{41}$$

plus

$$v_{\parallel 0} = -\frac{\alpha}{\Gamma_1 + \hat{Q}^2[\Gamma_2 + (4/3)\,\hat{\eta}_0] + \alpha}\frac{q}{r}\bar{v}_{\perp\theta}, \tag{42}$$

where

$$\alpha = \frac{3}{2}\frac{r^2}{q^2}\frac{\hat{\eta}_0 \Gamma_2}{\Gamma_2 + (4/3)\,\hat{\eta}_0}. \tag{43}$$

Thus,

$$\pi_{\parallel c} \simeq \frac{2}{3}\alpha\frac{q^2}{r^2}\bar{v}_{\perp r}, \tag{44}$$

$$\pi_{\parallel s} \simeq -\frac{2}{3}\alpha\frac{q^2}{r^2}\left(\frac{\Gamma_1 + \hat{Q}^2[\Gamma_2 + (4/3)\,\hat{\eta}_0]}{\Gamma_1 + \hat{Q}^2[\Gamma_2 + (4/3)\,\hat{\eta}_0] + \alpha}\right)\bar{v}_{\perp\theta}, \tag{45}$$

and

$$\epsilon_0^{-2}\langle \nabla\cdot\tilde{\mathbf{j}}_{\perp nc}\rangle \simeq -\frac{1}{r}\frac{d}{dr}\left[\rho\alpha\frac{q^2}{r^2}\left(\frac{\Gamma_1 + \hat{Q}^2[\Gamma_2 + (4/3)\,\hat{\eta}_0]}{\Gamma_1 + \hat{Q}^2[\Gamma_2 + (4/3)\,\hat{\eta}_0] + \alpha}\right) r\bar{v}_{\perp\theta}\right] + \mathrm{i}\frac{m}{r}\rho\alpha\frac{q^2}{r^2}\bar{v}_{\perp r}. \tag{46}$$

However,

$$\bar{v}_{\perp r} \simeq \mathrm{i}\,\gamma'\frac{m}{r}\bar{\phi}, \tag{47}$$

$$\bar{v}_{\perp\theta} \simeq -\gamma'\frac{d\bar{\phi}}{dr}, \tag{48}$$

to lowest order in ϵ_0, where $\tilde{\phi}(r,\theta,\varphi) = \bar{\phi}(r)\exp(i\zeta)$. It follows that

$$\epsilon_0^{-2}\langle \nabla\cdot\tilde{\mathbf{j}}_{\perp nc}\rangle \simeq \hat{\gamma}'\left[\frac{1}{r}\frac{d}{dr}\left(\rho\frac{q^2}{\epsilon_0^2}\hat{\mu}_\parallel\Gamma_\parallel r\frac{d\bar{\phi}}{dr}\right) - \frac{m^2}{r^2}\rho\frac{q^2}{\epsilon_0^2}\hat{\mu}_\parallel\Gamma_s\bar{\phi}\right], \tag{49}$$

where

$$\mu_\parallel = \frac{3}{2}\frac{\epsilon_0^4}{q^2}\frac{\eta_0}{\rho}, \tag{50}$$

$$\gamma_c = \frac{3}{4}\frac{\rho c_s^2}{\eta_0}, \tag{51}$$

$$\Gamma_s = \frac{\hat{\gamma}_c}{\hat{\gamma}_c + \hat{\gamma}'}, \tag{52}$$

$$\Gamma_\parallel = \frac{\Gamma_s[\Gamma_s(\hat{\gamma}' + \hat{\nu})\hat{\gamma}' + \epsilon_0^2 Q^2\hat{c}_s^2]}{\Gamma_s(\hat{\gamma}' + \hat{\nu})\hat{\gamma}' + \epsilon_0^2 Q^2\hat{c}_s^2 + \Gamma_s^2\hat{\gamma}'\hat{\mu}_\parallel r^2}, \tag{53}$$

and $\hat{\gamma}' = \epsilon_0^{-1}\gamma$, $\hat{\nu} = \epsilon_0^{-1}\nu$, $\hat{\gamma}_c = \epsilon_0^{-1}\gamma_c$, $\hat{\mu}_\parallel = \epsilon_0^{-1}\mu_\parallel$, and $\hat{c}_s = \epsilon_0^{-1}c_s$. By comparison, it is easily demonstrated that the divergence of the perturbed polarization current takes the form

$$\epsilon_0^{-2}\nabla\cdot\tilde{\mathbf{j}}_{\perp p} \simeq \hat{\gamma}'(\hat{\gamma}' + \hat{\nu})\left[\frac{1}{r}\frac{d}{dr}\left(\rho r\frac{d\bar{\phi}}{dr}\right) - \frac{m^2}{r^2}\rho\bar{\phi}\right]. \tag{54}$$

Thus, the divergences of the perturbed polarization and neoclassical currents can be combined to give

$$\epsilon_0^{-2}\nabla\cdot\tilde{\mathbf{j}}_{\perp p+nc} \simeq \frac{1}{r}\frac{d}{dr}\left[\rho\hat{\gamma}'\left(\hat{\gamma}' + \hat{\nu} + \frac{q^2}{\epsilon_0^2}\hat{\mu}_\parallel\Gamma_\parallel\right) r\frac{d\bar{\phi}}{dr}\right] - \frac{m^2}{r^2}\rho\hat{\gamma}'\left(\hat{\gamma}' + \hat{\nu} + \frac{q^2}{\epsilon_0^2}\hat{\mu}_\parallel\Gamma_s\right)\bar{\phi}. \tag{55}$$

I. Ideal eigenmode equation

Now $\tilde{\mathbf{b}}_\perp \simeq \nabla\tilde{\psi}\times\mathbf{n}$, to lowest order in ϵ_0, where $\tilde{\psi} = \mathrm{i}\epsilon_0 Q\tilde{\phi}$, Furthermore, $\tilde{j}_\parallel \simeq -\nabla^2\tilde{\psi}$, and

$$m\sigma = \frac{1}{r}\frac{d(r^2 Q)}{dr}. \tag{56}$$

It follows from Eq. (6) that

$$\nabla\cdot\tilde{\mathbf{j}} \simeq \mathbf{n}\cdot\nabla\tilde{j}_\parallel + \nabla\cdot\tilde{\mathbf{j}}_{\perp p+nc} + \epsilon_0\tilde{\mathbf{b}}_\perp\cdot\nabla\sigma = 0, \tag{57}$$

to lowest order in ϵ_0. Hence,

$$\epsilon_0^{-2}\nabla\cdot\tilde{\mathbf{j}}_{\perp p+nc} + Q\nabla^2(Q\bar{\phi}) - \frac{Q}{r}\frac{d}{dr}\left[\frac{1}{r}\frac{d(r^2 Q)}{dr}\right]\bar{\phi} \simeq 0, \tag{58}$$

which reduces to the desired eigenmode equation

$$r\frac{d}{dr}\left[\left(\rho\hat{\gamma}'\left[\hat{\gamma}' + \hat{\nu} + \frac{q^2}{\epsilon_0^2}\hat{\mu}_\parallel\Gamma_\parallel\right] + Q^2\right) r\frac{d\bar{\phi}}{dr}\right] - \left[m^2\left(\rho\hat{\gamma}'\left[\hat{\gamma}' + \hat{\nu} + \frac{q^2}{\epsilon_0^2}\hat{\mu}_\parallel\Gamma_s\right] + Q^2\right) + r\frac{dQ^2}{dr}\right]\bar{\phi} \simeq 0. \tag{59}$$

The above equation determines the radial plasma displace-

ment $\bar{\xi}(r) \propto \bar{\phi}(r)/r$ associated with an m,n RWM in the presence of plasma inertia, flow damping due to charge-exchange with neutrals, neoclassical flow damping, plasma compressibility, and sound waves.

Note that the conventional hydromagnetic time scale, $\tau_H = R_0\sqrt{\mu_0\rho_0}/B_z$, takes the value ϵ_0^{-1} in our normalization scheme. Thus, the parameters $\hat{\gamma}'$, $\hat{\mu}_\parallel$, $\hat{\nu}$, $\hat{\gamma}_c$, and $\hat{c}_s$, appearing in the above eigenmode equation, correspond to the dimensionless combinations $\gamma'\tau_H$, $(3/2)(\epsilon_0^4/q^2)(\eta_0/\rho\rho_0)(\tau_H/a^2)$, $\nu\tau_H$, $(3/4)(\Gamma P_0/\eta_0)\tau_H$, and $\sqrt{\Gamma P_0/\rho\rho_0}(\tau_H/a)$, respectively, where Γ is the plasma ratio of specific heats, and P_0 is the uniform background plasma pressure.

Finally, a *uniform* toroidal rotation of the plasma, with angular velocity Ω_ϕ, can be incorporated into the eigenmode equation by making the simple substitution

$$\gamma' \rightarrow \gamma + \mathrm{i}n\Omega_\phi, \tag{60}$$

where γ is the mode growth rate in the laboratory frame.

III. RESISTIVE WALL MODE DISPERSION RELATION

A. Vacuum region and wall

Suppose that the plasma is surrounded by a concentric, thin, uniform resistive wall of minor radius r_w. It is easily demonstrated that $\bar{\psi} \equiv Q\bar{\phi}$ satisfies

$$r\frac{d}{dr}\left(r\frac{d\bar{\psi}}{dr}\right) - m^2\bar{\psi} = 0 \tag{61}$$

in the vacuum region surrounding the plasma, subject to the matching constraint

$$\left[\frac{d\ln\bar{\psi}}{d\ln r}\right]_{r_{w-}}^{r_{w+}} = \hat{\gamma}\hat{\tau}_w \tag{62}$$

at the wall, and the physical boundary condition $\bar{\psi} \rightarrow 0$ as $r \rightarrow \infty$. Here, $\hat{\gamma} = \gamma\tau_H$, $\hat{\tau}_w = \tau_w/\tau_H$, and $\tau_w = \mu_0\sigma_w\delta_w r_w$, where σ_w is the wall electrical conductivity, and δ_w is the wall radial thickness.

B. Plasma response parameter

Launching a well-behaved solution of the ideal eigenmode Eq. (59) from the magnetic axis ($r=0$), and numerically integrating it to the edge of the plasma ($r=1$), we obtain the complex *plasma response parameter*

$$s(\hat{\gamma}) = -\frac{1}{2}\left(1 + m^{-1}\left.\frac{d\ln\bar{\psi}}{d\ln r}\right|_{r=1}\right). \tag{63}$$

C. RWM dispersion relation

Assuming that $\rho(r)$ and $\sigma(r)$ are zero at the edge of the plasma, it is easily demonstrated that $\bar{\psi}$ and $d\bar{\psi}/dr$ are both continuous across the plasma boundary. Hence, matching the plasma and vacuum solutions at $r=1$, we obtain the *resistive wall mode dispersion relation*[23]

$$\hat{\gamma}\left[c - (1-c)s(\hat{\gamma})\right] - \hat{\gamma}_w s(\hat{\gamma}) = 0. \tag{64}$$

Here, $\hat{\gamma}_w = 2m/\hat{\tau}_w$, and $c = r_w^{-2m}$. This dispersion relation can easily be solved numerically, via Newton iteration, to obtain the RWM growth rate, $\hat{\gamma}$, as a function of the various plasma and wall parameters.

D. Plasma stability parameter

The *marginally stable ideal eigenmode equation*,

$$r\frac{d}{dr}\left(Q^2 r\frac{d\bar{\phi}}{dr}\right) - \left(m^2Q^2 + r\frac{dQ^2}{dr}\right)\bar{\phi} \simeq 0, \tag{65}$$

is obtained from Eq. (59) by neglecting plasma inertia, and governs the stability of the ideal external-kink mode.[24] Calculating the plasma response parameter (63) from the above equation, we obtain a *real* number, s, which is equivalent to the well-known Boozer stability parameter for the ideal external-kink mode.[23] It can be demonstrated[23,24] that the m,n ideal external-kink mode is unstable in the absence of a wall (i.e., $\hat{\tau}_w \rightarrow 0$) when $s > 0$, and is unstable in the presence of a perfectly conducting wall (i.e., $\hat{\tau}_w \rightarrow \infty$) when $s > s_c \equiv c/(1-c)$. Hence, we can define a real *plasma stability parameter*

$$\bar{s} = \frac{s}{s_c}. \tag{66}$$

This parameter has the following properties. For $\bar{s} < 0$, the m, n ideal external-kink mode is stable. For $0 < \bar{s} < 1$, the m, n ideal external-kink mode is unstable in the absence of a wall, but stable in the presence of a perfectly conducting wall. Finally, for $\bar{s} > 1$, the m, n ideal external-kink mode is unstable even in the presence of a perfectly conducting wall. Thus, the *no-wall stability limit* corresponds to $\bar{s} = 0$, whereas the *perfect-wall stability limit* corresponds to $\bar{s} = 1$. Clearly, $\bar{s}$ is analogous to the figure of merit introduced in Eq. (1).

IV. THE HBT-EP TOKAMAK

A. Basic parameters

The HBT-EP tokamak,[17] is a circular cross section, large aspect ratio device which is ideally suited to the application of quasicylindrical RWM stability theory. The basic HBT-EP operation parameters are $R_0 = 0.92$ m, $a = 0.15$ m, $B_z = 0.35$ T, and $n_0 = 8 \times 10^{18}$ m^{-3}, where R_0 is the plasma major radius, a is the minor radius, B_z is the toroidal magnetic field strength on the magnetic axis, and n_0 is the central electron number density.[25] Thus, the inverse aspect ratio of the plasma is $\epsilon_0 \equiv a/R_0 = 0.163$. Furthermore, the hydromagnetic time scale is $\tau_H \equiv R_0\sqrt{\mu_0 n_0 m_p}/B_z \sim 3 \times 10^{-7}$ s.

Typical edge parameters for HBT-EP plasmas are $n_e \sim 2 \times 10^{18}$ m^{-3}, $T_i \sim 10$ eV, and $T_e \sim 20$ eV, where n_e is the edge electron number density, and T_i and T_e are the edge ion and electron temperatures, respectively. The typical neutral gas fill-pressure is $P_n = 3 \times 10^{-5}$ Torr.[25]

B. Equilibrium profiles

All of the RWM stability calculations presented in this paper are performed with the simple (normalized) density profile

$$\rho(r) = (1 - r^2)^{1/2}, \tag{67}$$

and the well-known Wesson q profile,[26]

$$q(r) = \frac{q_a r^2}{1 - (1 - r^2)^{q_a/q_0}}. \tag{68}$$

Here, q_0 is the value of the safety factor on the magnetic axis, whereas q_a is the value of the safety factor at the plasma boundary. It follows from Eqs. (2), (67), and (68) that $\rho=\sigma=0$ at the edge of the plasma, as was assumed in Sec. III C.

C. The HBT-EP wall

The HBT-EP wall[17] is unfortunately rather complicated, since it is made up of 10 separate (radially) movable toroidal segments, each only extending over the outboard side of the plasma. Five of the segments are fabricated from 1.2 cm (radially) thick aluminium, and the other five from 0.2 cm (radially) thick stainless steel. The aluminium and stainless steel segments alternate toroidally around the device. In the experiments discussed in this paper,[8,27] the stainless steel segments were all fully inserted (and were, hence, about 1 cm from the edge of the plasma), whereas the minor radius of the aluminium segments was varied from shot to shot, and was either greater than or equal to that of the stainless steel segments.

Making use of the analysis presented in Ref. 28, it is relatively straightforward to derive the generalization of the single-wall RWM dispersion relation (64) for the case where the plasma is surrounded by *two* thin, concentric, incomplete, nonoverlapping (in an angular sense), resistive walls. Suppose that the radius and time constant (i.e., $\mu_0\sigma\delta r$, where σ is the wall conductivity, δ is the wall radial thickness, and r is the wall minor radius) of the inner wall are r_1 and τ_1, respectively, whereas the corresponding quantities for the outer wall are r_2 and τ_2, respectively. Suppose, further, that the inner and outer walls extend over area fractions f_1 and f_2, respectively. (Thus, $f_1=1$ corresponds to a complete inner wall, and $f_1=0$ to no inner wall, etc.) The generalized RWM dispersion relation is written

$$\hat{\gamma}^2[c_{12} - s(\hat{\gamma})(1 - c_{12})] + \hat{\gamma}\{\hat{\gamma}_1[c_2 - s(\hat{\gamma})(1 - c_2)] + \hat{\gamma}_2[c_1 - s(\hat{\gamma})(1 - c_1)]\} - \hat{\gamma}_1\hat{\gamma}_2 s(\hat{\gamma}) = 0. \tag{69}$$

Here, $c_1=f_1 r_1^{-2m}$, $c_2=f_2 r_2^{-2m}$, $c_{12}=c_1+c_2$, $\gamma_1=2m/\tau_1$, $\gamma_2=2m/\tau_2$, $\hat{\gamma}_1=\gamma_1\tau_H$, and $\hat{\gamma}_2=\gamma_2\tau_H$. In this case. the critical value of the Boozer s parameter for instability of the ideal external-kink mode when both walls are perfectly conducting is $s_c=c_{12}/(1-c_{12})$.

Rather than making highly inaccurate estimates of the coupling coefficients, c_1 and c_2, and the wall growth rates, $\hat{\gamma}_1$ and $\hat{\gamma}_2$, from cylindrical theory (i.e., using the above formulas), we have instead elected to determine these parameters by fitting to data obtained from the VALEN code.[29] VALEN, which determines the RWM growth-rate as a function of the Boozer stability parameter, s, for a dissipationless plasma, models the HBT-EP wall segments in three dimensions via a finite-element representation which uses a standard thin-shell integral formulation. The plasma is represented as a surface current. The appropriate poloidal and toroidal distribution of this current over the plasma surface is calculated (for a predominately 3/1 external-kink mode in a plasma equilibrium with $q_0=1.4$ and $q_a=2.8$) from the ideal magnetohydrodynamical plasma stability code DCON.

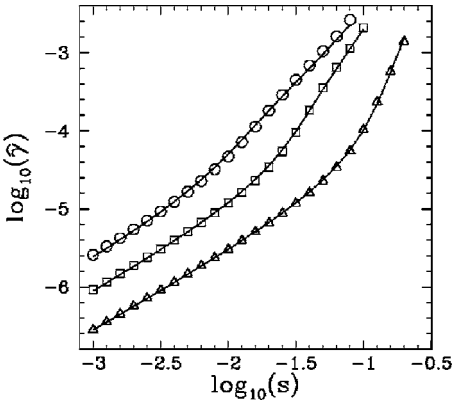

FIG. 1. The triangular, square, and circular points show the growth rate of the RWM (multiplied by $\tau_H=3\times10^{-7}$), as a function of the Boozer stability parameter, s, calculated from the VALEN code for HBT-EP, with the stainless steel segments of the wall all fully inserted, and the aluminium segments all retracted by 0 cm, 4 cm, and 8 cm, respectively. The corresponding curves show fits of the two-wall RWM dispersion relation (69) to these data. The fitting parameters are given in Table I.

Figure 1 and Table I give the results of fitting the two-wall RWM dispersion relation (69) (with s real) to VALEN data for three different HBT-EP wall configurations. It can be seen that the VALEN data are very well represented by the dispersion relation, provided, of course, that appropriate choices are made for the fitting parameters c_1, c_2, $\hat{\gamma}_1$, and $\hat{\gamma}_2$. Note that our fitting procedure *uniquely* determines the value of each of these parameters. Incidentally, the VALEN data cannot be accurately fitted by the single-wall RWM dispersion relation (64), no matter what choices are made for the values of the fitting parameters c and $\hat{\gamma}_w$.

D. Charge-exchange flow damping

HBT-EP plasmas are characterized by a relatively high edge density of cold neutrals. Moreover, charge-exchange reactions between plasma ions and neutrals leads to a strong

TABLE I. The fitting parameters used to generate Fig. 1. Here, d is the retraction distance of the aluminium segments of the HBT-EP wall. Also shown is the effective plasma-wall coupling constant $c_{12}=c_1+c_2$, and the critical Boozer stability parameter, $s_c\equiv c_{12}/(1-c_{12})$, for ideal instability when the walls are perfectly conducting. Note that $\tau_H\sim3\times10^{-7}$ s.

d(cm)	c_1	c_2	$\hat{\gamma}_1\equiv\gamma_1\tau_H$	$\hat{\gamma}_2\equiv\gamma_2\tau_H$	c_{12}	s_c
0	1.36×10^{-1}	1.09×10^{-1}	1.75×10^{-3}	3.11×10^{-5}	0.245	0.325
4	1.22×10^{-1}	3.49×10^{-2}	2.38×10^{-3}	3.27×10^{-5}	0.157	0.186
8	1.19×10^{-1}	1.45×10^{-2}	2.63×10^{-3}	3.99×10^{-5}	0.134	0.154

damping of ion rotation in the outer regions of the plasma.[12,13] Assuming, as seems reasonable, that any momentum gain of neutrals due to charge-exchange is promptly lost to the walls, the (unnormalized) damping rate is approximately

$$\nu \sim v_i n_n \sigma_x, \tag{70}$$

where $v_i \equiv \sqrt{T_i/m_p}$ is the ion thermal velocity, n_n is the number density of neutrals, and σ_x is the charge-exchange cross section. The latter quantity takes the value

$$\sigma_x \simeq 7 \times 10^{-19}[1 - 0.155 \log_{10} T_i]^2 \ \mathrm{m}^2 \tag{71}$$

in a hydrogen plasma, where T_i is the ion temperature (in eV).[30] The edge neutral density can be estimated from the neutral fill-pressure, $P_n = n_n T_n$. Here, the neutral temperature T_n is assumed to be about 20 °C.

Estimating the normalized charge-exchange flow-damping rate at the edge of a typical HBT-EP plasma, we obtain $\hat{\nu} \equiv \nu \tau_H \sim 5.2 \times 10^{-3}$.

E. Neoclassical flow damping

Neoclassical flow damping is a magnetic pumping effect which arises because of the inevitable poloidal variation of the magnetic field strength around flux surfaces in a toroidal plasma.[14] The expression for the flow-damping parameter used in this paper is [see Eq. (50)]

$$\mu_\parallel = \frac{3}{2}\frac{\epsilon_0^4}{q^2}\frac{\eta_0}{\rho}, \tag{72}$$

where ϵ_0 is the inverse aspect ratio, q is the safety factor, ρ is the plasma mass density, and η_0 is the parallel ion viscosity.[19] Now, this expression is only valid in the so-called *collisional* regime, in which the ion collision frequency, ν_i (defined in Ref. 19), exceeds the ion transit frequency, $\nu_t = v_i/(R_0 q)$.[16] Estimating these quantities at the edge of a typical HBT-EP plasma, we find that the ratio $\nu_* = \nu_i/\nu_t$ is approximately 4. Hence, we are justified in employing Eq. (72).

Estimating the normalized neoclassical flow-damping parameter at the edge of a typical HBT-EP plasma, we obtain $\hat{\mu}_\parallel \equiv \mu_\parallel(\tau_H/a^2) \sim 3.6 \times 10^{-5}$. Likewise, estimating the (normalized) sound speed, $\hat{c}_s = c_s(a/\tau_H)$, and the (normalized) plasma compressibility parameter, $\hat{\gamma}_c \equiv \gamma_c \tau_H$ [see Eq. (51)], at the edge of a typical HBT-EP plasma, we get $\hat{c}_s \sim 0.16$ and $\hat{\gamma}_c \sim 6.3 \times 10^{-2}$, respectively.

F. RWM stability in HBT-EP

When the stainless steel and aluminium segments of the HBT-EP wall are all fully inserted, the naturally occurring level of toroidal rotation in HBT-EP plasmas (i.e., $\Omega_\phi/2\pi \sim 5$ kHz, which corresponds to $\hat{\Omega}_\phi \equiv \Omega_\phi \tau_H \sim 0.01$) is found to be sufficient to stabilize the RWM virtually all of the way up to the perfect-wall stability limit (i.e., up to $\bar{s} \sim 1$).[8,27] On the other hand, if the aluminium segments are all fully retracted, then the naturally occurring plasma rotation is found to be insufficient to stabilize the RWM all of the way up to the perfect wall stability limit.

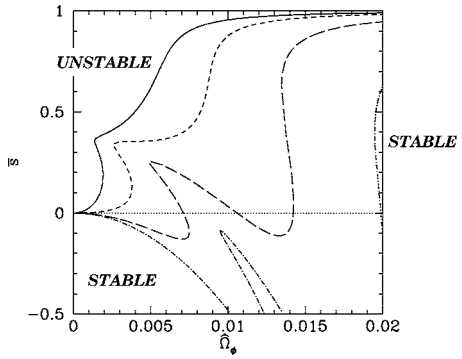

FIG. 2. Stability boundaries for the RWM in normalized plasma rotation versus plasma stability space, calculated from the simplified ideal eigenmode Eq. (73), the RWM dispersion relation (69), the wall parameters given in Table I (*for* $d=0$ cm), and the equilibrium profiles (67) and (68). The calculation parameters are $m=3$, $n=1$, and $q_a=2.95$. The solid, short-dashed, long-dashed, and dotted-dashed curves correspond to $\hat{\nu}=0.02$, 0.01, 5×10^{-3}, and 2.5×10^{-3}, respectively. The no-wall and perfect-wall stability limits lie at $\bar{s}=0$ and $\bar{s}=1$, respectively.

V. DISSIPATION DUE TO CHARGE-EXCHANGE WITH NEUTRALS

Let us neglect neoclassical flow damping (by setting $\hat{\mu}_\parallel$ to zero). In this limit, the ideal eigenmode Eq. (59) simplifies considerably to give

$$r\frac{d}{dr}\left[(\rho\hat{\gamma}'[\hat{\gamma}' + \hat{\nu}] + Q^2)r\frac{d\bar{\phi}}{dr}\right] - \left[m^2(\rho\hat{\gamma}'[\hat{\gamma}' + \hat{\nu}] + Q^2) + r\frac{dQ^2}{dr}\right]\bar{\phi} \simeq 0. \tag{73}$$

Figure 2 shows the RWM stability boundary in normalized plasma rotation (i.e., $\hat{\Omega}_\phi \equiv \Omega_\phi \tau_H$) versus plasma stability (i.e., $\bar{s}$) space, determined using the simplified ideal eigenmode Eq. (73), the two-wall RWM dispersion relation (69), the wall parameters given in Table I, and the equilibrium profiles specified in Sec. IV B. The calculations are performed for an $m=3/n=1$ mode whose rational surface lies just outside the plasma (i.e., $q_a=2.95$), and an HBT-EP wall with the stainless steel and aluminium segments all fully inserted (corresponding to $d=0$ cm in Table I). The plasma stability parameter $\bar{s}$ is varied by varying q_0. The stability boundary is determined for various values of the normalized charge-exchange flow-damping parameter, $\hat{\nu}$. Note that, although the calculation is performed with $\hat{\nu}$ constant throughout the plasma, the value of $\hat{\nu}$ should be regarded as characterizing the strength of the flow damping at the *edge* of the plasma, since it is only at the edge of the plasma (where Q becomes very small) that dissipative processes have any effect on the RWM. The same caveat applies to the other dissipation mechanism discussed in this paper.

It can be seen, from Fig. 2, that when the dissipation is relatively large (i.e., $\hat{\nu}=0.02$), the RWM is completely stable below the no-wall stability boundary (i.e., $\bar{s}<0$). Above the no-wall boundary (i.e., $\bar{s}>0$), the RWM is unstable when $\hat{\Omega}_\phi$ lies below some critical value. Note that the critical value of $\hat{\Omega}_\phi$ required to stabilize the RWM goes to zero as $\bar{s}\to 0$, and

the RWM consequently becomes stable, and goes to infinity as $\bar{s}\rightarrow 1$, and the ideal external-kink mode consequently becomes unstable.

As the dissipation is reduced, the critical value of $\hat{\Omega}_\phi$ required to stabilize the RWM increases, and the stability curve starts to dip below the no-wall stability boundary (see the $\hat{\nu}=5\times 10^{-3}$ curve), indicating the presence of a band (or bands) of $\hat{\Omega}_\phi$ values, below the no-wall limit, within which the RWM is destabilized by plasma rotation.[11] When the dissipation is relatively small (i.e., $\hat{\nu}=2.5\times 10^{-3}$), the region of instability below the no-wall limit becomes very extensive, and a relatively large value of $\hat{\Omega}_\phi$ is required to stabilize the RWM above the no-wall limit.

Note that the strong indentations in the stability boundaries shown in Fig. 2 correspond to the regions of parameter space where the aluminium segments of the wall switch from having an effectively resistive response (at low $\hat{\Omega}_\phi$ values) to an effectively perfectly conducting (at high $\hat{\Omega}_\phi$ values) response to the RWM.

Now, the RWM is not generally seen in HBT-EP plasmas below the no-wall limit. Moreover, the RWM is observed to be stabilized above the no-wall limit, up to $\bar{s}\simeq 1$, by the naturally occurring levels of plasma rotation (i.e., $\hat{\Omega}_\phi\simeq 0.01$). From Fig. 2, these observations imply that if flow damping due to charge-exchange with cold neutrals is to provide the requisite plasma dissipation in HBT-EP, then the normalized damping rate, $\hat{\nu}$, needs to be at least 0.01. However, our earlier estimate for $\hat{\nu}$ was 5×10^{-3}, which is 2 times smaller than the required value. Hence, we conclude that edge dissipation due to charge-exchange with neutrals is not quite large enough an effect to account for the observed rotational stabilization of the RWM in HBT-EP plasmas.

VI. DISSIPATION DUE TO NEOCLASSICAL FLOW DAMPING

Let us neglect flow damping due to charge-exchange (by setting $\hat{\nu}$ to zero), plasma compressibility (by setting Γ_s to unity), and sound waves (by setting c_s to zero). In this limit, the ideal eigenmode Eq. (59) simplifies to give[15]

$$r\frac{d}{dr}\left[\left(\rho\hat{\gamma}'^2\left[1+\frac{q^2}{\epsilon_0^2}\frac{\hat{\mu}_\parallel}{\hat{\gamma}'+\hat{\mu}_\parallel r^2}\right]+Q^2\right)r\frac{d\bar{\phi}}{dr}\right] - \left[m^2\left(\rho\hat{\gamma}'\left[\hat{\gamma}'+\frac{q^2}{\epsilon_0^2}\hat{\mu}_\parallel\right]+Q^2\right)+r\frac{dQ^2}{dr}\right]\bar{\phi}\simeq 0. \tag{74}$$

Figure 3 shows the RWM stability boundary in normalized plasma rotation versus plasma stability space, determined using the simplified ideal eigenmode Eq. (74), the two-wall RWM dispersion relation (69), the wall parameters given in Table I, and the equilibrium profiles specified in Sec. IV B. The calculations are performed for an $m=3/n=1$ mode whose rational surface lies just outside the plasma (i.e., $q_a=2.95$), and an HBT-EP wall with the stainless steel and aluminium segments all fully inserted (corresponding to $d=0$ cm in Table I). The stability boundary is determined for various values of the normalized neoclassical flow damping parameter, $\hat{\mu}_\parallel$.

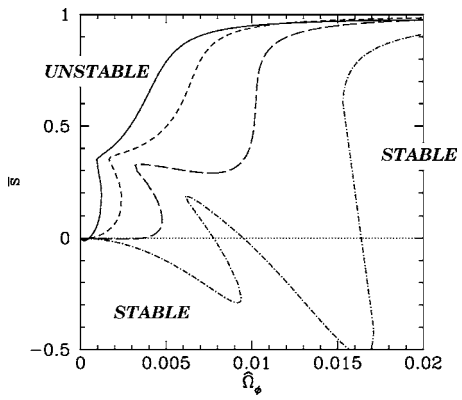

FIG. 3. Stability boundaries for the RWM in normalized plasma rotation versus plasma stability space, calculated from the simplified ideal eigenmode Eq. (74), the RWM dispersion relation (69), the wall parameters given in Table I (for $d=0$ cm), and the equilibrium profiles (67) and (68). The calculation parameters are $m=3$, $n=1$, $q_a=2.95$, and $\epsilon_0=0.163$. The solid, short-dashed, long-dashed, and dotted-dashed curves correspond to $\hat{\mu}_\parallel=1\times 10^{-4}$, 5×10^{-5}, 2.5×10^{-5}, and 1.25×10^{-5}, respectively. The no-wall and perfect-wall stability limits lie at $\bar{s}=0$ and $\bar{s}=1$, respectively.

It can be seen that as the neoclassical flow damping parameter, $\hat{\mu}_\parallel$, is reduced, the stability boundaries evolve in much the same manner as those shown in Fig. 2. Moreover, it is clear, from Fig. 3, that if dissipation via neoclassical flow damping is to account for the observed stabilization of the RWM in HBT-EP (i.e., a rotation rate of $\hat{\Omega}_\phi\simeq 0.01$ sufficient to stabilize the RWM up to $\bar{s}\sim 1$) then $\hat{\mu}_\parallel$ needs to be between 2.5×10^{-5} and 5×10^{-5}, or larger. However, our earlier estimate for $\hat{\mu}_\parallel$ was 3.6×10^{-5}. Hence, we conclude that dissipation due to edge neoclassical flow damping is just about large enough of an effect to account for the observed rotational stabilization of the RWM in HBT-EP plasmas.[15]

We can determine the effect of plasma compressibility and sound waves on the RWM stability boundaries shown in Fig. 3 by allowing γ_c [defined in Eq. (51)] and c_s (the sound speed) to take finite values. We estimate that $\hat{\gamma}_c=\gamma_c\tau_H$ and $\hat{c}_s=c_s(\tau_H/a)$ are approximately 6.3×10^{-2} and 0.16, respectively, at the edge of a typical HBT-EP plasma. It turns out that the RWM stability boundaries calculated using these values are indistinguishable from those shown in Fig. 3 (which are calculated with $\hat{\gamma}_c=\infty$ and $\hat{c}_s=0$). Hence, we conclude that plasma compressibility and sound waves both have a *negligible* effect on the stability of the RWM in HBT-EP plasmas.

VII. THE RWM STABILITY BOUNDARY

Figures 4 and 5 show the RWM stability boundary in HBT-EP calculated using our best guesses for the values of the dissipation parameters (i.e., $\hat{\nu}\sim 5\times 10^{-3}$, $\hat{\mu}_\parallel\sim 3.6\times 10^{-5}$, $\hat{c}_s\sim 0.16$, and $\hat{\gamma}_c\sim 6.3\times 10^{-2}$).

Figure 4 illustrates how the stability boundary evolves as the aluminium segments of the HBT-EP wall are retracted. (Note that $\bar{s}=s/s_c$, in this figure, where $s_c=0.325$ is the critical s value calculated when the aluminium segments are *fully*

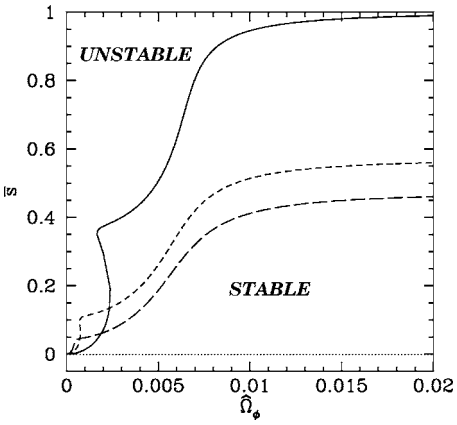

FIG. 4. Stability boundaries for the RWM in normalized plasma rotation versus plasma stability space, calculated from the full ideal eigenmode Eq. (59), the RWM dispersion relation (69), the wall parameters given in Table I, and the equilibrium profiles (67) and (68). The calculation parameters are $m=3$, $n=1$, $q_a=2.95$, $\epsilon_0=0.163$, $\hat{\nu}=5\times10^{-3}$, $\hat{\mu}_\parallel=3.6\times10^{-5}$, $\hat{\gamma}_c=6.3\times10^{-2}$, and $\hat{c}_s=0.16$. The solid, short-dashed, and long-dashed curves correspond to the cases where the aluminium segments of the wall are retracted by 0 cm, 4 cm, and 8 cm, respectively. Here, $\bar{s}\equiv s/s_c$ is the Boozer stability parameter normalized with respect to $s_c=0.325$, which is the critical stability parameter for the case where the aluminium segments are fully inserted.

inserted, see Table I.) It can be seen that when the aluminium segments of the HBT-EP wall are all fully inserted, the edge dissipation present in HBT-EP plasmas is sufficient for the naturally occurring levels of plasma rotation (i.e., $\hat{\Omega}_\phi\sim0.01$) to stabilize the RWM most of the way up to the perfect-wall stability limit (i.e., up to $\bar{s}\sim1$). However, when the aluminium segments are all retracted, the RWM can only be stabilized about half of the way up to the perfect-wall stability limit (i.e., up to $\bar{s}\sim0.5$).

Figure 5 shows how the RWM stability boundary evolves as q_a is varied. It is clear that the RWM becomes harder to stabilize as q_a falls further below the resonant value 3, and vice versa.

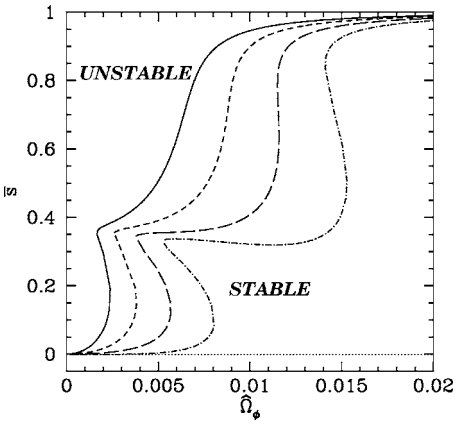

FIG. 5. Stability boundaries for the RWM in normalized plasma rotation versus plasma stability space, calculated from the full ideal eigenmode Eq. (59), the RWM dispersion relation (69), the wall parameters given in Table I (for $d=0$ cm), and the equilibrium profiles (67) and (68). The calculation parameters are $m=3$, $n=1$, $\epsilon_0=0.163$, $\hat{\nu}=5\times10^{-3}$, $\hat{\mu}_\parallel=3.6\times10^{-5}$, $\hat{\gamma}_c=6.3\times10^{-2}$, and $\hat{c}_s=0.16$. The solid, short-dashed, long-dashed, and dotted-dashed curves correspond to $q_a=2.95$, 2.94, 2.93, and 2.92, respectively. The no-wall and perfect-wall stability limits lie at $\bar{s}=0$ and $\bar{s}=1$, respectively.

VIII. SUMMARY

We have derived a relatively simple model of the RWM in a large aspect ratio, low β, circular cross section, tokamak plasma, surrounded by a concentric, thin, uniform resistive wall. Our model assumes *uniform* toroidal plasma rotation (for the sake of simplicity), and includes the following realistic *edge* dissipation mechanisms: dissipation due to charge-exchange with cold neutrals, and dissipation due to neoclassical flow damping.[15]

We have applied our model to the HBT-EP tokamak, determining the wall parameters by fitting to data from the VALEN code.[29] We find that edge dissipation due to charge-exchange with cold neutrals is not quite large enough an effect to account for the observed rotational stabilization of the RWM in HBT-EP plasmas. On the other hand, edge dissipation due to neoclassical flow damping is (just about) large enough to explain the observations. Taking both dissipation mechanisms together, we conclude that the net edge dissipation in HBT-EP plasmas is certainly sufficient to account for the observed rotational stabilization of the RWM.

ACKNOWLEDGMENTS

The authors would like to thank David Maurer, Mike Mauel, and Bill Rowan for helpful discussions during the preparation of this paper.

This research was funded by the U.S. Department of Energy under Contract No. DE-FG05-96ER-54346.

[1] F. Troyon, R. Gruber, H. Saurenmann, S. Semenzato, and S. Succi, Plasma Phys. Controlled Fusion **26**, 209 (1984).
[2] C. Kessel, J. Manickam, G. Rewoldt, and W. M. Tang, Phys. Rev. Lett. **72**, 1212 (1994).
[3] E. A. Lazarus, G. A. Navratil, C. M. Greenfield *et al.*, Phys. Rev. Lett. **77**, 2714 (1996).
[4] J. P. Goedbloed, D. Pfirsch, and H. Tasso, Nucl. Fusion **12**, 649 (1972).
[5] M. Okabayashi, N. Pomphrey, J. Manikam *et al.*, Nucl. Fusion **36**, 1167 (1996).
[6] A. M. Garofalo, E. Eisner, T. H. Ivers *et al.*, Nucl. Fusion **38**, 1029 (1998).
[7] S. A. Sabbagh, J. M. Bialek, R. E. Bell *et al.*, Nucl. Fusion **44**, 560 (2004).
[8] M. Shilov, C. Cates, R. James *et al.*, Phys. Plasmas **11**, 2573 (2004).
[9] A. Bondeson, and D. J. Ward, Phys. Rev. Lett. **72**, 2709 (1994).
[10] R. Betti, and J. P. Freidberg, Phys. Rev. Lett. **74**, 2949 (1995).
[11] R. Fitzpatrick, Phys. Plasmas **9**, 3459 (2002).
[12] W. L. Rowan, A. G. Meigs, E. R. Solano, P. M. Valanju, M. D. Calvin, and R. D. Hazeltine, Phys. Fluids B **5**, 2485 (1993).
[13] E. D. Taylor, C. Cates, M. E. Mauel, D. A. Maurer, D. Nadle, G. A. Navratril, and M. Shilov, Phys. Plasmas **9**, 3938 (2002).
[14] T. H. Stix, Phys. Fluids **16**, 1260 (1973).
[15] K. C. Shaing, Phys. Plasmas **11**, 5525 (2004).
[16] J. A. Wesson, *Tokamaks*, 3rd ed. (Oxford University Press, Oxford, 2004).
[17] T. Ivers, E. Eisner, A. Garofalo *et al.*, Phys. Plasmas **3**, 1926 (1996).
[18] J. P. Freidberg, *Ideal Magnetohydrodynamics* (Springer, New York, 1987).
[19] S. I. Braginskii, "Transport processes in a plasma," in *Reviews of Plasma Physics* (Consultants Bureau, New York, 1965), Vol. 1, p. 205.
[20] R. D. Hazeltine and J. D. Meiss, *Plasma Confinement* (Dover, New York, 2003).
[21] J. D. Callen, W. X. Qu, K. D. Siebert *et al.*, in *Plasma Physics and Controlled Nuclear Fusion Research 1986 Proceedings of the 11th Conference, Kyoto* (International Atomic Energy Agency, Vienna, 1987), Vol. 2, p. 157.
[22] A. I. Smolyakov and E. Lazzaro, Phys. Plasmas **11**, 4353 (2004).
[23] A. H. Boozer, Phys. Plasmas **5**, 3350 (1998).

[24]W. A. Newcomb, Ann. Phys. (N.Y.) **10**, 232 (1960).
[25]D. Maurer and M. E. Mauel (private communication, 2006).
[26]J. A. Wesson, Nucl. Fusion **18**, 87 (1978).
[27]M. E. Mauel, J. Bialek, A. H. Boozer, *et al.*, Nucl. Fusion **45**, 285 (2005).
[28]R. Fitzpatrick, Phys. Plasmas **1**, 2931 (1994).
[29]J. Bialek, A. H. Boozer, M. E. Mauel, and G. A. Navratil, Phys. Plasmas **8**, 2170 (2001).
[30]A. C. Riviere, Nucl. Fusion **11**, 363 (1971).